Drug delivery into microneedle-porated nails from nanoparticle reservoirs

Wing Sin Chiu [a], Natalie A. Belsey [a,1], Natalie L. Garrett [b], Julian Moger [b], Gareth J. Price [c], M. Begoña Delgado-Charro [a], Richard H. Guy [a,*]

[a] Department of Pharmacy & Pharmacology, University of Bath, Claverton Down, Bath BA2 7AY, UK
[b] Department of Physics & Medical Imaging, University of Exeter, Exeter EX4 4QL, UK
[c] Department of Chemistry, University of Bath, Claverton Down, Bath BA2 7AY, UK

ARTICLE INFO

ABSTRACT

This study demonstrates the potential of polymeric nanoparticles as drug reservoirs for sustained topical drug delivery into microneedle-treated human nail. Laser scanning confocal microscopy was used to image the delivery of a fluorescent model compound from nanoparticles into the nail. A label-free imaging technique, stimulated Raman scattering microscopy, was applied, in conjunction with two-photon fluorescence imaging, to probe the disposition of nanoparticles and an associated lipophilic 'active' in a microneedle-porated nail. The results provide clear evidence that the nanoparticles function as immobile reservoirs, sequestered on the nail surface and in the microneedle-generated pores, from which the active payload can be released and diffuse laterally into the nail over an extended period of time.

© 2015 Elsevier B.V. All rights reserved.

1. Introduction

Conventional topical nail formulations have limited usefulness, due to both immobilization of the drug once the volatile solvent in the formulation has evaporated, and the low diffusivity of drug across the compact keratinized structure of the nail plate. There is therefore a need for better, more effective formulations for the treatment of nail diseases such as onychomycosis and nail psoriasis. Polymeric nanoparticles (NPs) have been proposed as constituents of topical formulations to act as drug reservoirs from which sustained delivery into skin and hence increased local bioavailability can be achieved [1–3]. The potential for using NPs in some way as components of topical nail formulations is essentially unexplored, however, and there is a need for research in the area to assess their potential and provide an underpinning scientific understanding to optimize their use.

On the skin, the highly convoluted surface, and the entrances to appendageal structures, such as follicles, offer sites at which NPs can accumulate, giving long residence times during which release of their drug payload is possible [4,5]. In contrast, the nail surface has a relatively more homogeneously smooth topography and is self-evidently not perforated by hairs or sweat glands. To provide sites in the nail into which drug-loaded NPs can be sequestered, pre-treatment with a microneedle array is considered here. This 'poration' approach has been the subject of intensive study with respect to drug delivery into and through skin, where piercing the stratum corneum creates new, low-resistance pathways through which the active may gain facile and rapid access to the underlying viable epidermis (and, ultimately, the systemic circulation) [6]. While it is unlikely that a microneedle array can completely penetrate through the nail, fissures can be created into which NPs may be deposited, and from which a prolonged and slow release of an active can occur. A key component of the research is visualization of the disposition of the NPs and their associated 'active' payload following topical application to the nail. The resulting information will provide useful support for the further development and optimization of topical nail formulations.

In the first part of the study, a fluorescent probe, Nile Red (molecular weight = 318.4 Da; calculated log P = 4.07 ± 0.26 [7]) was incorporated into the NPs, and laser scanning confocal microscopy was employed to visualize its disposition following topical application to intact and microneedle-porated nails. In the second part, two-photon fluorescence and stimulated Raman scattering microscopies were used in combination to probe the fates of fluorescently-tagged NPs and an associated lipophilic 'active', octyl methoxycinnamate (molecular weight = 290.4 Da; calculated log P = 5.18 ± 0.65 [7]), in microneedle-porated nails.

* Corresponding author.
  E-mail address: r.h.guy@bath.ac.uk (R.H. Guy).
[1] Current address: National Physical Laboratory, Hampton Road, Teddington, Middlesex, TW11 0LW, UK

2. Materials and methods

2.1. Chemicals

ε-Caprolactone, preformed poly-(ε-caprolactone) (PCL) (MW ~10,000), polysorbate 85 (Tween 85), Nile Red (NR) (analytical grade), octyl methoxycinnamate (OMC), tin(II) 2-ethylhexanoate (stannous octoate), propylene glycol (PG) and isopropyl myristate (IPM) were obtained from Sigma-Aldrich Co. (Gillingham, UK). 5,10,15,20-tetrakis-(4-aminophenyl)porphyrin (TAPP) was obtained from Tokyo Chemical Industry Co. (Tokyo, Japan).

2.2. Nail sample preparation

Human fingernail clippings (at least 8 mm in length) were obtained from healthy volunteers who gave informed consent. Ethical approval was granted by the Research Ethics Approval Committee for Health (REACH; EP 11/12 115) of the University of Bath. Nails were stored at −20 °C until used. Prior to the experiments, the nail was soaked in deionized water for 30 min to restore some flexibility. Microporation was performed using a commercially available dermaroller (Infinitive Beauty, Birmingham, UK), comprising 250 μm long titanium needles, which was applied to the dorsal side of the hydrated nail by rolling it back and forth a total of 5 times.

2.3. Synthesis of TAPP-labelled PCL

Star-shaped PCL with a TAPP core was synthesized [8] by introducing TAPP (0.025 mmol), stannous octoate (0.0025 mmol) and ε-caprolactone (0.7 g) into a 10 mL round-bottom flask under argon. After polymerization with stirring for 72 h at 110 °C, the cooled product was dissolved in dichloromethane and precipitated by dropwise addition to cold stirred methanol. The precipitated TAPP-PCL was filtered and dried at 40 °C. ^1H NMR spectra in deuterated chloroform (CDCl$_3$) were recorded on a Bruker Avance™ III spectrometer (Billerica, MA, USA) operating at 400 MHz.

2.4. NP preparation

NR-loaded PCL NPs were prepared by the solvent displacement method [9]. An acetone solution (10 mL) containing 5 mg of NR and 125 mg of preformed PCL was injected drop-wise into 50 mL of an aqueous solution containing 3% (w/v) Tween 85. NPs were formed rapidly, creating an opalescent suspension. The acetone was removed under reduced pressure and the NP suspension was further concentrated to a final volume of 20–30 mL, which was then filtered (0.45 μm nylon filters, Whatman, Maidstone, UK) to remove any aggregates. TAPP-labelled NPs loaded with OMC were prepared using the same procedure but replacing preformed PCL and NR with TAPP-PCL and OMC (5.1% w/v in the organic phase), respectively.

2.5. NP characterization

Nanoparticle size and polydispersity index were measured in triplicate using dynamic light scattering (ZetaSizer Nano S, Malvern, UK), following a 100-fold dilution of the suspension.

The morphology of the NPs was imaged using transmission electron microscopy (TEM) (JEM-2000, JEOL Ltd., Tokyo, Japan) at an accelerating voltage of 120 kV. Each specimen was prepared by drop-casting the NP suspension onto a carbon coated copper grid, which was then cryo-desiccated before imaging.

The amount of NR or OMC entrapped in the NPs was calculated from the difference between the quantity found after complete dissolution of the particles in acetonitrile (Q_{tot}), and that in the aqueous supernatant (Q_{sup}) after ultrafiltration–centrifugation of the suspension at 6000 rpm for 30 min (MWCO 3000, Millipore Corp., Watford, UK). All experiments were performed in triplicate. The entrapment efficiency (%) was given by: $\{100 \times [(Q_{tot} - Q_{sup}) / Q_{input}]\}$, where Q_{input} represents the input amount.

2.6. In vitro release of NR from the NP suspension

NR release from the NPs into an oil phase was quantified in a membrane-less system. 0.5 mL of an aqueous NP suspension was placed in an Eppendorf tube and 4.5 mL of isopropyl myristate (IPM) was added. The system was constantly stirred and the NR content of the IPM was measured at fixed time intervals. The release of NR from a solution in PG (at the equivalent NR concentration as in the NP suspension) was performed as a positive control.

To obtain the solubility of NR in IPM, a saturated solution was prepared by stirring excess solute into the solvent over a period of 48 h. The final suspension was then filtered through a nylon membrane (pore size = 0.45 μm) and the concentration of NR in the filtrate was quantified by HPLC (n = 3).

NR was assayed by HPLC with fluorescence detection (Dionex, Sunnyvale, CA, USA). A HiQ sil C18W 250 × 4.6 mm column (KYA Tech, Tokyo, Japan) was employed and the mobile phase was methanol–water (95:5) at a flow rate of 1 mL/min. The excitation and emission wavelengths were set at 559 nm and 630 nm, respectively. The injection volume was 20 μL and the system was maintained at 25 °C. The NR retention time was 6.5 min. The limits of detection and quantification were 12.7 and 38.6 ng/mL, respectively.

OMC concentrations were quantified using HPLC (Jasco, Great Dunmow, UK) with UV detection at 310 nm. A mobile phase consisting of acetonitrile–water (85:15) at pH 2.5 (adjusted using orthophosphoric acid) was pumped at 1 mL/min through an Acclaim® 120 C18 150 × 4.6 mm column (Dionex, Sunnyvale, CA, USA). The injection volume was 10 μL and the retention time was 9.5 min. The limits of detection and quantification were calculated as 2.6 μg/mL and 7.9 μg/mL, respectively.

2.7. In vitro nail permeation

NR uptake into intact (non-porated) nail was first evaluated in vertical Franz diffusion cells (PermeGear Inc., Bethlehem, PA, USA, diffusion area = 0.2 cm^2). The nail was mounted with the dorsal surface facing the donor chamber; the ventral side was fully hydrated by contact with phosphate buffered saline (pH 7.4) in the receptor chamber. 300 μL of the NP aqueous suspension was introduced into the donor compartment, which was covered with Parafilm® to avoid evaporation. The entire diffusion cell was then placed in an incubator at 32 °C. Nails treated with deionized water served as negative controls. After 7 days, the diffusion cell was dismantled and excess formulation at the surface was removed gently with absorbent tissue. The nail was then immediately examined by LSCM.

NR uptake as a function of time into microneedle-porated nail was measured after application of 10 μL of the NP suspension onto the dorsal surface. The samples were then sandwiched between two glass coverslips and sealed securely with double-sided tapes and Parafilm® to avoid evaporation. Confocal images of the selected regions of interest were recorded as a function of time. Control experiments were performed in the same way using non-porated nails.

2.8. Laser scanning confocal microscopy (LSCM)

An inverted laser-scanning microscope (510Meta, Carl Zeiss, Jena, Germany) was used. A HeNe laser (543 nm) was employed to excite NR and the emission signals were collected using a LP 560 filter. Planar (x–y) and cross-sectional confocal images were captured to assess the localization of the fluorophore on or within the nail. Dorsal images were acquired using an oil objective (EC Plan-Neo 40×/1.3 M27, Carl Zeiss). To obtain a direct transverse view of the nail, an air objective

(Plan-Apochromat 10×/0.45 M27, Carl Zeiss) was employed. In this case, the treated nail was thinly sectioned and the slices were then glued to a microscope slide with the cross-section orientated towards the objective. All transverse images were recorded from a few microns below the cut surface to avoid any artefact caused by the sectioning. To rule out interference from any nail auto-fluorescence, the laser power and detector settings were minimized so that no signal was detectable from the untreated negative control. Reflectance and/or optical images were captured.

2.9. Raman spectroscopy

The Raman spectra of OMC and of a human nail sample were recorded (Renishaw RM1000 Raman microscope and v1.2 WIRE software, Renishaw plc, Wotton-Under-Edge, UK). A 1200-line/mm grating providing spectral resolution of 1 cm^{-1} was used with a diode laser at 785 nm with up to 300 mW power. The Raman band (520 cm^{-1}) of a silicon wafer was used for calibration. The Vancouver Raman Algorithm (BC Cancer Agency & University of British Columbia, Canada) was used to remove the fluorescence background from the Raman spectra.

2.10. Stimulated Raman scattering (SRS) and two-photon fluorescence (TPF) imaging

The distribution of OMC and TAPP-PCL NPs on and within the microneedle-porated nail was determined after either a 3-hour or 7-day application. The nails were mounted in the diffusion cells as described above and 10 μL of an aqueous NP suspension was applied to an area of approximately 0.2 cm^2. Before imaging, the samples were sandwiched between two glass coverslips and sealed securely with double-sided tape and Parafilm® to avoid evaporation.

SRS and TPF imaging [10,11] were carried out sequentially using a picosecond laser system and a custom modified commercial inverted microscope with a confocal laser scanner (FV300/IX71, Olympus UK Ltd., UK). The laser system consisted of a Nd-Vanadium laser (picoTRAIN, High-Q GmbH) that delivered a 7 ps pulse train at a 76 mHz repetition rate. A portion of the output provided the pump laser fundamental (1064 nm). The remainder of the output was frequency-doubled and was used to synchronously pump an optical parametric oscillator (OPO) (Levante Emerald, APE, Berlin) at 532 nm. The OPO consisted of a temperature-tuned, non-critically phase matched Lithium Triborate (LBO) crystal, which allows the OPO signal to be continuously tuned from 690 to 980 nm by adjusting the LBO temperature and an intercavity Lyot filter. A Si PIN photodiode was used to record the intensity variations of the OPO signal. The pump laser fundamental and the OPO signal were used as the Stokes and pump beams, respectively. Before entering the microscope, the 1064 nm Stokes beam was amplitude modulated at 1.7 MHz with an acousto-optic modulator (3080–197 Crystal Technologies, West Chester, PA, US). The pump beam and the modulated Stokes beam were spatially overlapped using a dichroic mirror (1064 DCRB, Chroma Technology Corp, Bellows Falls, US) and temporally overlapped using a delay stage. The collinear beams were then directed into the microscope and focussed onto the sample using a 60 × 1.2 NA water immersion objective (UPlanSApo, Olympus) and scanned in two dimensions using a pair of galvanometer mirrors. The laser power at the sample was attenuated to below 40 mW in total.

The resulting stimulated Raman loss (SRL) in the pump beam was collected in the forward direction via a 1.0 NA condenser lens (LUMFI, Olympus) and detected by a large area photodiode (FDS1010, Thorlabs, New Jersey, USA). A band-pass filter (850/90 nm, Chroma) was mounted in front of the detector to block the modulated 1064 nm beam. Finally, a lock-in amplifier (SR844, Stanford Research Systems, Sunnyvale, CA, USA) was employed to detect the SRL signal with a time constant of 30–100 μs. The output "R" from the lock-in was used to generate the SRL images.

TPF was excited using the OPO signal output at 816 nm with the 1064 nm beam shuttered. The signal was collected in the epi-direction and detected by a photomultiplier tube (R3896, Hamamatsu, Hertfordshire, UK). The absence of nail autofluorescence under the conditions used was confirmed by imaging a control, untreated nail sample.

2.11. Image analysis

All images acquired were processed using ImageJ (U.S. National Institutes of Health, Bethesda, MD, USA). Fluorescence signal quantification at various nail depths was performed using the 'specify' and 'plot profile' plugins in ImageJ. Each SRS data point was normalized against the OPO signal recorded from the PIN photodiode to correct for the laser intensity fluctuations. Images of different Raman shifts and/or TPF fluorescence signal were presented using different colour schemes for ease of interpretation.

3. Results and discussion

3.1. Poly-(ε-caprolactone) (PCL) NPs loaded with Nile Red (NR)

3.1.1. NP characterization

The average NP diameter was 152 ± 3 nm with a relatively small polydispersity index of 0.15 ± 0.01; the individual particles were spherical (Fig. S1). The encapsulation efficiency of NR in the polymeric NPs was 89 ± 1%, a result consistent with other studies [9,12], which have reported similarly high loading efficiencies of lipophilic compounds. No free NR was detected in the suspension presumably due to the compound's very low water solubility. The final NR concentration in the nano-suspension was 206 ± 2 μg/mL.

3.1.2. In vitro release of NR

IPM is a good solvent for NR and was therefore selected as a receptor medium. The solubility of NR in IPM was found to be 379 ± 8 μg/mL and the concentrations measured in the release study were always less than one-tenth of this value confirming that sink conditions were maintained. The cumulative (%) release of NR from a solution in PG, and from a polymeric NP suspension (Fig. S2) was 80% within 3 h for the former whereas for the NPs, this level of release was achieved only after 12 h. The release of NR from the NPs comprised a faster component during the first 3 h attributable presumably to the relatively rapid dissociation of surface-bound NR, followed by a slower component controlled by diffusion of the entrapped marker from within the polymer matrix.

3.2. LSCM imaging

3.2.1. In vitro uptake of NR into non-porated nails

The distribution of NR on or within the non-porated nail after the application of the NP suspension for 7 days was examined using LSCM. Images of 3 representative nail samples from three different volunteers are shown in Fig. 1. Cross-sectional (x–z) reconstructions of the sequentially acquired planar (x–y) images (both reflectance and fluorescence signals) (Fig. 1a,b) show an intense, bright red band of fluorescence from NR on and within the superficial part of the nail, with a measurable signal perceptible down to depths of approximately 70–90 μm. These observations are consistent with the direct, transverse visualization of mechanically sectioned nail slices (Fig. 1c–e). It follows that, over 7 days, NR was released from the NPs and successfully permeated into the nail plate to a depth corresponding to only about 30% of its total thickness.

The transport pathway of NR across the nail may also be identified. Fig. 2 provides illustrative x–y planar images of an example, showing the reflectance signal and NR fluorescence at approximately 10 μm, 20 μm and 30 μm depths into the nail. The reflectance images reveal the fairly regular polyhedral, squamoid shape of the onychocytes that
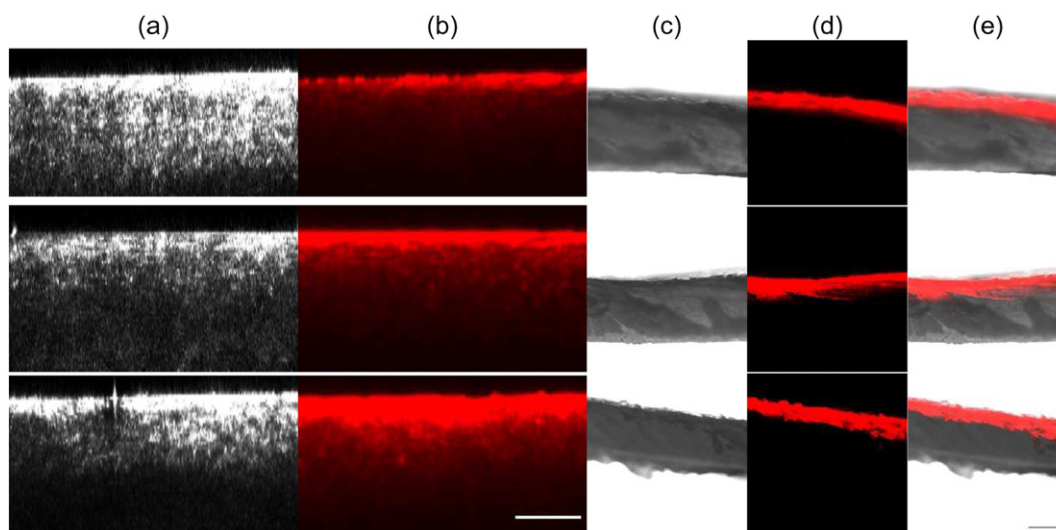
Fig. 1. Representative images of nail cross-sections, either reconstructed from confocal x–y sections (a, b), or transversally sectioned (c–e), following 7-day application of PCL-NR NPs. Panel (a): reflectance signal from the nail plate. Panels (b) and (d): NR fluorescence. Panel (c): optical micrographs. Panel (e): merged images of (c) and (d). Scale bar = 50 µm (a, b) and 200 µm (c–e).

measure about 30 µm across [13,14]. Localization of NR at the intercellular regions was clearly visible, a point reinforced by the simultaneously acquired fluorescence images. As expected, the hydrophobic NR has high affinity for these more lipid-rich domains, even though the total lipid content of the nail plate is low (0.1–1%) [15]. Indeed, the permeation of lipophilic compounds has been considered unfavourable, despite suggestions that transport, in fact, has little dependence on a drug's lipophilicity [16,17], and the identification of transport pathways remains an open question. Nonetheless, the nail plate is known to contain phospholipid, particularly in the dorsal and ventral layers [18], and the intercellular spaces (25–35 nm) are reported to be filled with a 'mortar' that contains membrane-coating granules comprised primarily of phospholipids [19]. These domains may therefore provide a sympathetic environment for small, hydrophobic molecules and constitute a potential lipophilic pathway for nail permeation. However, it should be noted that a recent work [20] investigated the iontophoretic penetration of fluorescent markers, sodium fluorescein and Nile blue chloride, into the nail and the results supported a transcellular pathway. The apparent difference observed in the current study may suggest different penetration pathways for iontophoretic and passive transport. Further investigation is therefore necessary to elucidate these findings and to elucidate unequivocally the contribution of each pathway to nail

permeation. Finally, bright (i.e., NR-stained) punctate features were also observed, increasing in number with depth into the nail and may correspond to nuclear remnants (retained shrunken or fragmented nuclei), also known as 'pertinax bodies' [21].

3.2.2. In vitro uptake of NR into non-porated and porated nails as a function of time

Subsequently, the disposition of NR following application of a PCL NP suspension to both non-porated and microneedle-porated nails was assessed as a function of time; the results are shown in Fig. 3. For intact nails, the most intense signal remains at the surface where the NP formulation is localized; however, as time progresses, release and penetration of NR produce a slowly increasing level of fluorescence in deeper regions of the nail (Fig. 3a).

The impact of microneedle poration is evident from the distinctly different images seen in Fig. 3b. When the microneedle device is rolled back and forth over the nail surface, not only are rectangular-shaped pores created, but unavoidable scratch marks are also made. While there is still intense NR fluorescence at the nail surface, there is also a large signal from within the pores at short time post-application, demonstrating that the NPs fill the pores. Images acquired at later times reveal both the release of NR from the NP 'reservoirs' on the surface and within the pores and its penetration into the nail, from the sides of the pores. As observed above, intercellular NR penetration is also apparent here in nails that have been microneedle-porated.

The average pixel intensity data extracted from the images as a function of time and position are presented graphically in Fig. 3c and d. The data represent the mean ($\pm$ standard deviation), and reflect the variability observed across five randomly sampled regions (25×25 µm^2) of the nail; in the microneedle-treated nail these sites were at least 10 µm from the pore edge. Notably, and self-evidently, no significant uptake of NR into the intact nail had occurred during the experiment. In contrast, the time-dependent diffusion of NR into the microneedle-porated nail is clearly indicated. The insets to Fig. 3c and d plot the corresponding areas under the respective pixel intensity versus nail depth profiles (AUC). For the intact nail, there is no difference whatsoever between the AUCs at any of the measurement times (repeated measures ANOVA, $p > 0.05$); in contrast, for the microneedle-treated nail, there is a significant difference between all the measured AUCs except those determined at 24 and 48 h (repeated measures ANOVA followed by Bonferroni post hoc test; $p < 0.05$). As hypothesized, therefore, the microneedle-created pores in the nail fulfil a similar role to that
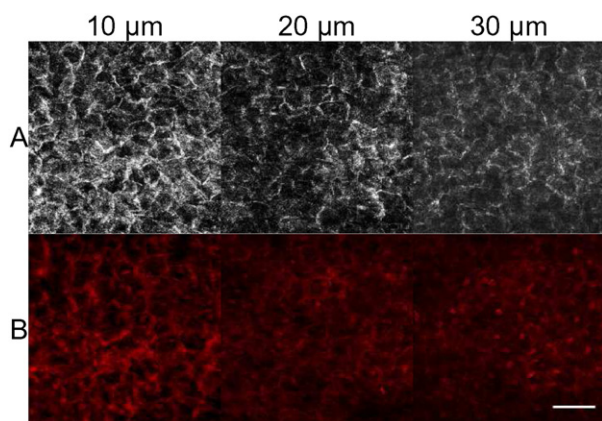

Fig. 2. Planar images (x–y) of NR disposition in a nail at depths 10, 20 and 30 µm: (A) reflectance signal; (B) NR fluorescence. Scale bar = 50 µm.
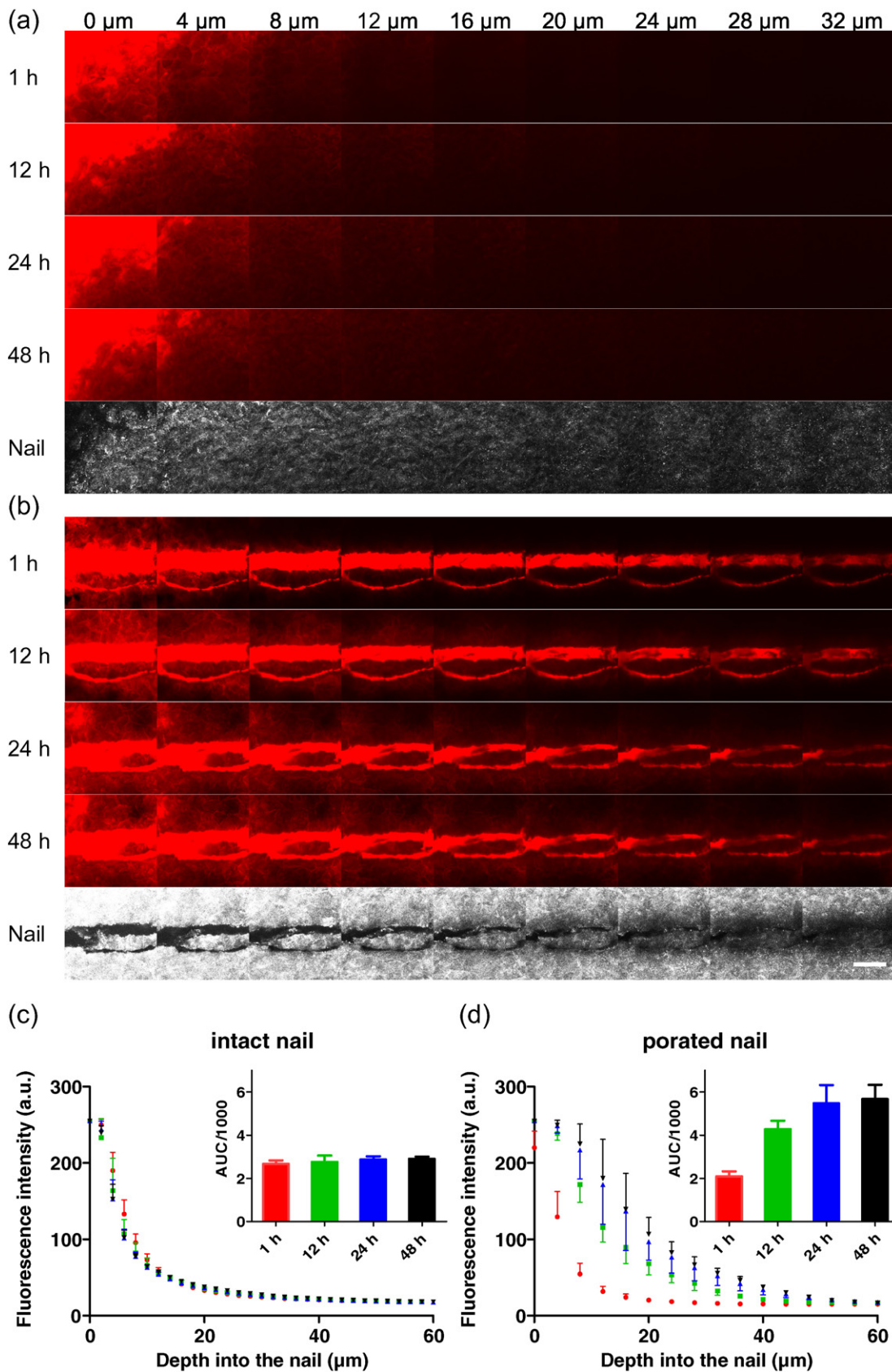
Fig. 3. LSCM visualization of NR disposition as functions of time and depth into (a) intact, and (b) microneedle-porated, nails. Scale bar = 50 μm. Fluorescence signal versus nail depth profiles for (c) intact and (d) microneedle-porated nails as a function time post-application. These data represent the mean (±SD) of the fluorescent signal from 5 randomly selected sites (25 × 25 μm²) on the nail. In the case of the microneedle-porated nail, the sampled areas were at least 10 μm from the pore. The insets show the areas under the respective pixel intensity versus nail depth profiles (AUC; mean + SD); no significant difference (p > 0.05) for intact nail, significant difference (p < 0.05; repeated measures ANOVA followed by Bonferroni post hoc test) observed between all time points in the porated nail, except 24 h and 48 h.

described for skin furrows and hair follicles when NP formulations are applied topically to the skin [22], in addition to shortening the diffusion path-length of the penetrant once released from the carrier.

In further support of this conclusion, the reconstructed x–z orthogonal image of a non-porated nail (Fig. 4a) recorded 48 h after the start of the experiment reveals an intense signal from the NP formulation at the surface and that NR, which has been released, has penetrated ~25 μm into the nail plate. In contrast, the corresponding images from a microneedle-porated nail (Fig. 4a) show not only the presence of large amounts of NPs at the surface but that they have also filled the pore and gained access to the nail down to a depth of ~70 μm. Moreover, a red 'haze' in the surrounding nail tissues is clearly observed indicating that enhanced, lateral NR release has taken place.

Fig. 4b provides semi-quantitative support for this conclusion and presents the average fluorescence signal across the orthogonal images as a function of depth into the nails. While the signal at 0–10 μm originates primarily from the superficial formulation layer in both samples, the fluorescence rapidly falls to baseline with increasing depth into the intact nail. The signal profiles from the porated nail manifest strong fluorescence peaks within the pore. While the regions distant from the pore show rapid signal decay with depth, those close to the pore reveal the presence of a more substantial fluorescence, confirming the evident lateral diffusion of NR.

Overall, these results reveal how NPs deliver their payload into the microneedle-porated nail. The long residence time of NR fluorescence on the nail surface and within the pore attests to the non-penetrability of the NPs themselves across the barrier, as has been inferred in a number of publications reporting their 'fate' on the skin [3–5]. The diffusion of fluorescence, increasing with time and distance from the surface/pore supports the release of NR from the NPs and its subsequent penetration into the nail. Absolute confirmation, nonetheless, requires both particle and penetrant to be simultaneously and unambiguously tracked, a challenge that is now addressed using TPF and SRS imaging in combination.

3.3. TAPP-tagged PCL NPs loaded with OMC

3.3.1. Fluorescently-tagged NP synthesis

The reactant fluorophore, TAPP acted as an initiator during the stannous octoate-catalysed polymerization of ε-caprolactone. The ^{1}H NMR spectrum of the TAPP-PCL (Fig. S3), indicated that TAPP was covalently bound to PCL. This was essential for interpretation of the TPF imaging, confirming that the detected TAPP fluorescence originated only from NPs, the disposition of which could therefore be tracked unambiguously.

3.3.2. NP characterization

The TAPP-PCL NPs entrapped OMC, a lipophilic UV filter commonly used in topical sunscreen products. OMC was chosen because (a) it serves as a reasonable model for terbinafine (molecular weight = 291.4 Da; log P = 5.52 ± 0.30 (7)), a drug frequently used in the treatment of onychomycosis, and (b) it is known to be efficiently loaded into polymeric NPs [23,24] due, at least in part, to its high lipophilicity. Furthermore, OMC is a liquid at room temperature and can itself act as the oil phase in the nanoprecipitation process. The average NP diameter was 136 ± 1 nm with a polydispersity index of 0.26 ± 0.01; individual particles were spherical (Fig. S1b). The final OMC concentration in the suspension was 17.8 ± 0.4 mg/mL and the encapsulation efficiency was 96 ± 2%.

3.3.3. SRS and TPF imaging

The Raman spectra of OMC and of a nail sample (Fig. S4) show that the absorbance centred at 1600 cm^{-1} originating from aromatic C—C bond stretching can be used to identify OMC. Although TAPP may also give rise to a small signal at the same frequency, the fluorophore can be uniquely identified and differentiated from OMC using TPF.

The disposition of OMC and TAPP-PCL on and within the microneedle-porated nail following application of the NP suspension for 3 h and 7 days was imaged by SRS and TPF microscopies. SRS was tuned sequentially to 2855 cm^{-1} to image (principally) the —CH$_2$ bond stretching vibration
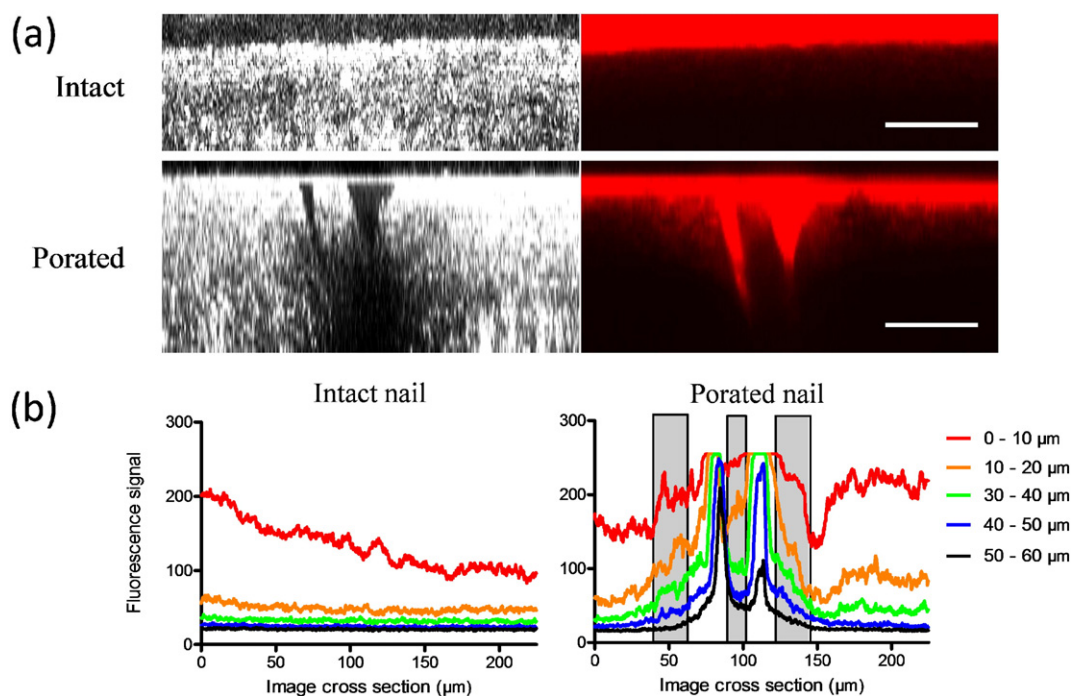

Fig. 4. (a) Reconstructed cross-sectional images recorded 48 h after application of NR-loaded PCL NPs to intact and microneedle-porated nails as a function of depth. Left panel: reflectance signals from the nail plate. Right panel: NR fluorescence. Scale bars = 50 μm. (b) NR fluorescence signal intensity profiles recorded 48 h after the start of the experiment across the orthogonal images (in Fig. 4a) of intact and microneedle-porated nails. The right panel represents the corresponding depths into the nail. Grey highlighted areas indicate regions immediately surrounding the pores.

from the nail, 1802 cm^{-1} to record any off resonance background, and 1600 cm^{-1} to image the aromatic C—C stretch from OMC. As reported recently [11], the use of perdeuterated compounds would mean that the —CH$_2$ signal would originate uniquely from the nail. However, this assignment is less specific here because both OMC (Fig. S4) and the PCL polymer also include —CH$_2$ groups in their structures and contribute therefore to this resonance. The off-resonance signal verified that there was essentially no background when the laser was tuned away from the target vibrational resonances. Only an extremely low endogenous signal from the nail and the occasional punctate 'spots' due to two-photon absorption [25] from residual dirt particles on the nail surface were detected. TPF microscopy was used to locate the fluorescently-tagged NPs. The x–y planar images (236 μm × 236 μm) were captured in 2 μm depth increments (but are shown here only every 4 μm for clarity). The scan time for each frame was 18.4 s. The aromatic C—C

signal could have originated from both OMC and TAPP, as mentioned before, but the TPF signal allowed specific and unequivocal imaging of the NPs.

Fig. 5 shows the x–y planar images of SRS and TPF signals obtained at different depths into the nail pre-treated with a microneedle roller. The rectangular, 'trench-like' structures created are clearly visible. At 3 h post-application, the images confirm the co-location of the aromatic C—C signal (OMC) and the TAPP fluorescence both on the nail surface and within the pores. The overlaid images reveal essentially perfect alignment of the signals at all imaging depths and that minimal separation of OMC from the NPs is apparent on this short time-scale.

After 7 days, while the fluorescence from the NPs remains exclusively confined to the nail surface and within the pores, the SRS signal from OMC indicates its release from the NPs and subsequent diffusion away from the surface/pore into the nail.
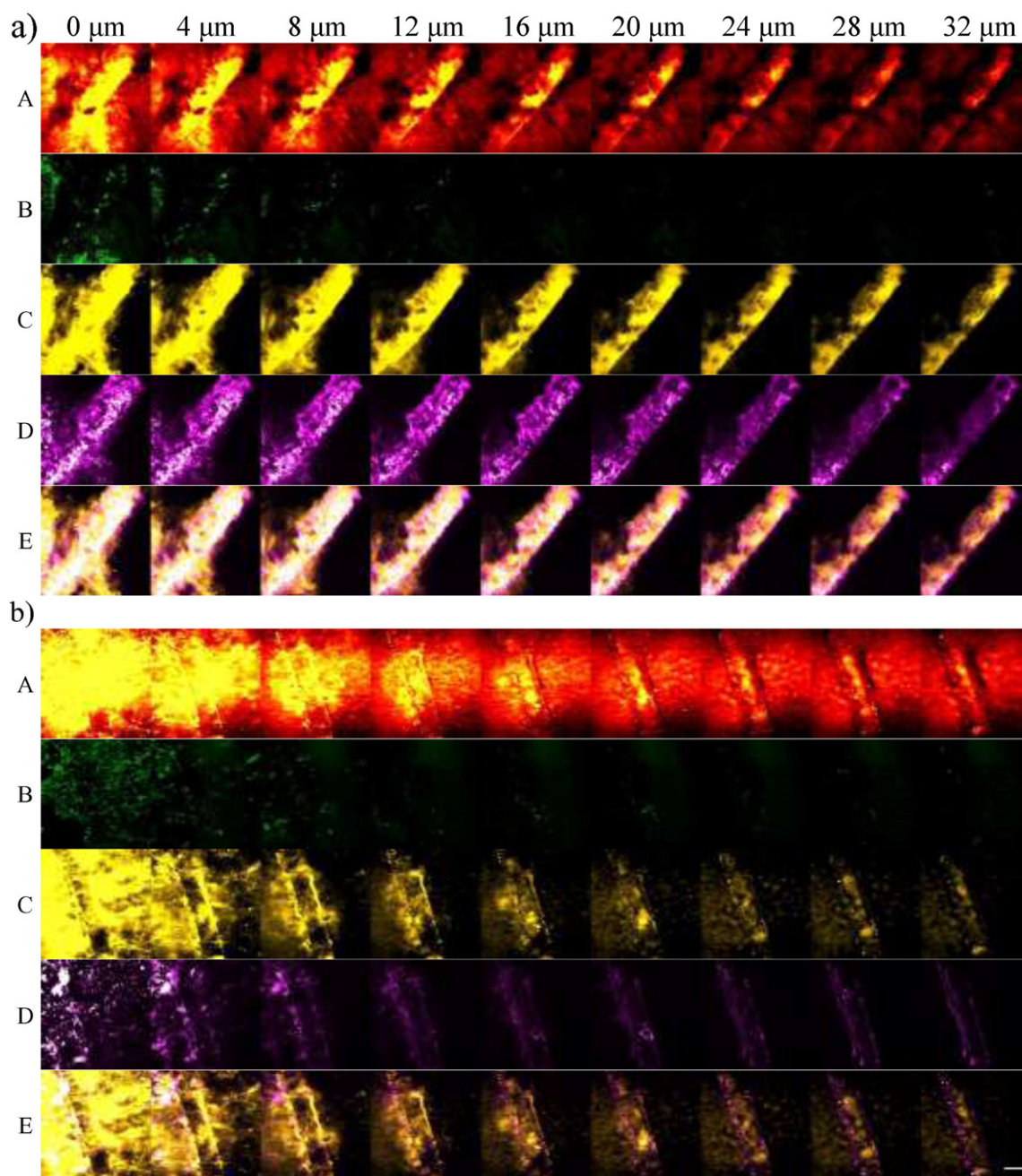

Fig. 5. SRS (panels A–C) and TPF (panel D) images recorded as a function of depth after (a) 3 h, and (b) 7 days, application of OMC-loaded, fluorescently-tagged NPs to microneedle-porated nails. (A) —CH$_2$ resonance primarily from the nail. (B) Off-resonance signal. (C) Aromatic C—C vibration from OMC. (D) TPF from the NPs. (E) Overlay of panels C and D. Scale bar = 50 μm.
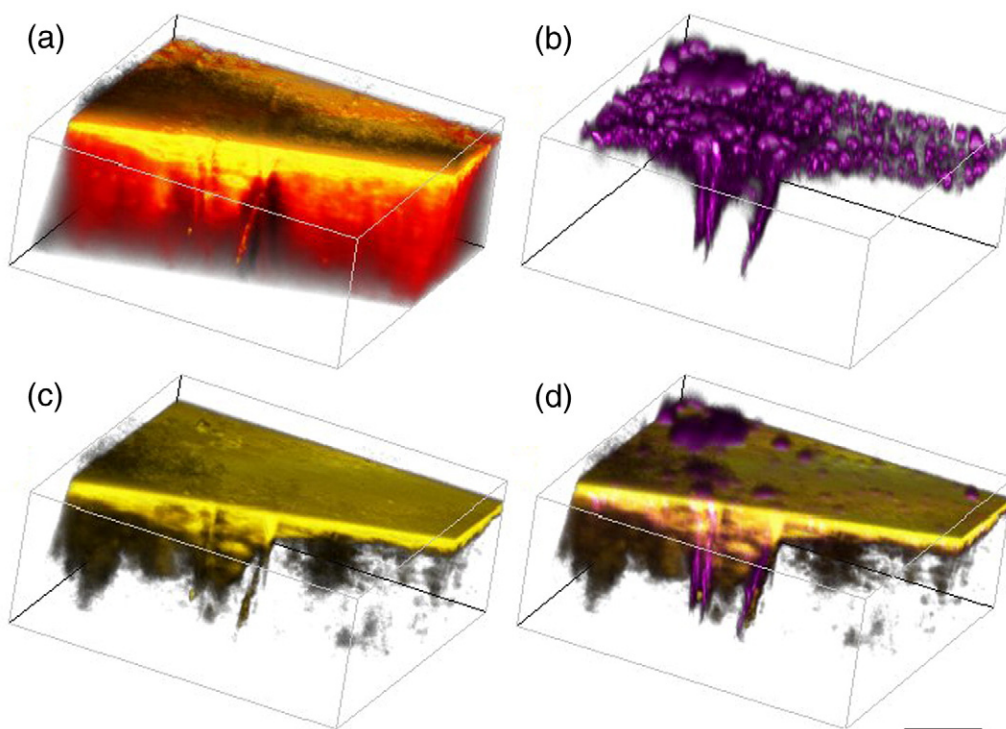
Fig. 6. Three-dimensional reconstruction (prepared using ImageJ 'volume viewer' plugin) of a representative microneedle-created pore, 7 days post-application of a NP suspension onto the porated nail, showing the distribution of (A) $-CH_2$ resonance primarily from the nail; (B) TPF from the NPs; (C) aromatic C—C signal from OMC; and (D) overlay of panels B and C. Scale bar = 50 μm.

Fig. 6 illustrates the three-dimensional reconstruction of a representative microneedle-created 'trench' that enables direct visualization of the NPs and OMC. Notably, the fluorescence signal from the NPs is visibly intense on the nail surface and within the internal confines of the 'trench', but no penetration of the NPs beyond these boundaries has occurred. In contrast, the diffusion of OMC (denoted by the SRS aromatic C—C signal) into the nail is clearly indicated, supporting the separation of the active from the NPs and its permeation into and through the nail.

The average pixel intensity data extracted from the TPF images of TAPP and the SRS images of OMC as a function of time and nail depth are presented graphically in Fig. 7a and b, respectively. As was done with the LSCM images for Nile Red, the data represent the mean (+ standard deviation) across five different regions (25×25 μm^2) of the nail; once again, in the microneedle-treated nail these sites were at least 10 μm from the pore edge. While the TAPP signal profiles measured at 3 h and at 7 days post-application align perfectly as a function of nail depth, the OMC signal at 7 days is clearly separated from that observed at 3 h, confirming the release of the compound from the NPs and diffusion into the surrounding nail matrix. The insets to Fig. 7a and b show the corresponding areas under the respective signal versus nail depth profiles (AUC). For the NPs (i.e., TAPP), there is no difference whatsoever between the AUCs at 3 h and at 7 days; in contrast, for OMC, and in support of the above conclusion, the AUC is significantly greater at 7 h ($p < 0.05$).

Taken together, the SRS and TPF images clearly confirm that, 7 days post-application, OMC has been released into and has started to diffuse within the nail while the fluorescently-tagged NPs remain confined to the surface and within the pores. These results concur with the images obtained previously where the release of NR from unlabelled NPs was inferred from confocal microscopy imaging. The data presented here
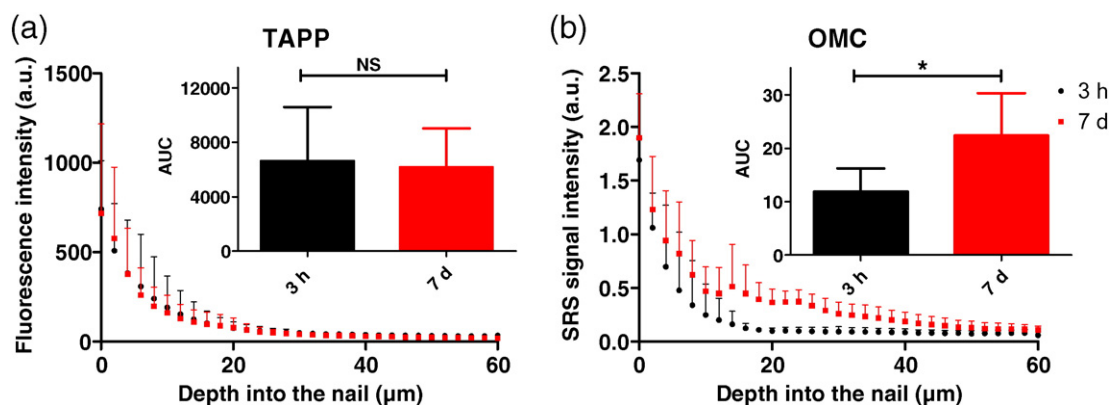

Fig. 7. Fluorescence and SRS signal versus nail depth profiles for (a) TAPP and (b) OMC, respectively, at 3 h and 7 days post-application (n = 5, mean + SD). These data represent the mean (+SD) of the corresponding signals from 5 randomly selected sites (25×25 μm^2) on the nail. In the case of the microneedle-porated nail, the sampled areas were at least 10 μm from the pore. The insets show the areas under the respective signal versus nail depth profiles (AUC; mean + SD); for TAPP, NS = no significant difference ($p > 0.05$) whereas, for OMC, *indicates a significant difference ($p < 0.05$; two-tailed, unpaired t-test).

confirm this deduction unambiguously: the NPs do indeed act as immobile reservoirs, sequestered on the nail and in the physically created pores, sustaining the prolonged release of an active payload over an extended period of time.

4. Conclusions

In the first part of this study, a lipophilic fluorophore, Nile Red (NR), was encapsulated into poly (ε-caprolactone) nanoparticles and its distribution following topical application to intact nail and nail porated with microneedles was imaged using laser scanning confocal microscopy. Post-application to the nail, sustained release of NR was observed. Subsequently, using stimulated Raman scattering and two-photon fluorescence microscopies, release of the lipophilic octyl methoxycinnamate from fluorescently-labelled nanoparticles into microneedle-porated nail was demonstrated. The images and their semi-quantitative analysis showed that microneedle-created pores (a) provided sequestration sites for the NPs from which the associated compound is released over a period of several days, and (b) permitted lateral diffusion of 'active' to occur more rapidly into the deeper regions of the nail. Over the same time, in contrast, no movement of NPs was perceptible. The results provide clear evidence that NPs can function as reservoirs for lipophilic compounds and sustain their local release over a period of several days.

Finally, with respect to the translation of this research to clinical practice, the present study is clearly a 'proof-of-concept' rather than a demonstration of direct feasibility. There are obviously technological barriers to overcome in putting together a user-friendly and economically viable medicinal product that combines some form of nail poration (or partial poration) with a controlled drug delivery reservoir. This does not, of course, constrain one to using microneedles for the former or nanoparticles for the latter, and exploration of other approaches are certainly warranted at this time.

Supplementary data to this article can be found online at http://dx. doi.org/10.1016/j.jconrel.2015.10.026.

Acknowledgements

References

[1] R. Alvarez-Roman, A. Naik, Y.N. Kalia, R.H. Guy, H. Fessi, Skin penetration and distribution of polymeric nanoparticles, J. Control. Release 99 (2004) 53–62.

[2] S.S. Guterres, M.P. Alves, A.R. Pohlmann, Polymeric nanoparticles, nanospheres and nanocapsules, for cutaneous applications, Drug Targ. Insights 2 (2007) 147–157.

[3] J. Luengo, B. Weiss, M. Schneider, A. Ehlers, F. Stracke, K. Konig, K.H. Kostka, C.M. Lehr, U.F. Schaefer, Influence of nanoencapsulation on human skin transport of flufenamic acid, Skin Pharmacol. Physiol. 19 (2006) 190–197.

[4] C.S. Campbell, L.R. Contreras-Rojas, M.B. Delgado-Charro, R.H. Guy, Objective assessment of nanoparticle disposition in mammalian skin after topical exposure, J. Control. Release 162 (2012) 201–207.

[5] F. Stracke, B. Weiss, C.M. Lehr, K. Konig, U.F. Schaefer, M. Schneider, Multiphoton microscopy for the investigation of dermal penetration of nanoparticle-borne drugs, J. Investig. Dermatol. 126 (2006) 2224–2233.

[6] T.M. Tuan-Mahmood, M.T. McCrudden, B.M. Torrisi, E. McAlister, M.J. Garland, T.R. Singh, R.F. Donnelly, Microneedles for intradermal and transdermal drug delivery, Eur. J. Pharm. Sci. 50 (2013) 623–637.

[7] ALOGPS, 2.1 program, VCCLAB, Virtual Computational Chemistry Laboratory, http://www.vcclab.org2005.

[8] L.Z. Zhang, Y. Lin, Y.J. Zhang, R. Chen, Z.S. Zhu, W. Wu, X.Q. Jiang, Fluorescent micelles based on star amphiphilic copolymer with a porphyrin core for bioimaging and drug delivery, Macromol. Biosci. 12 (2012) 83–92.

[9] R. Alvarez-Román, A. Naik, Y.N. Kalia, R.H. Guy, H. Fessi, Enhancement of topical delivery from biodegradable nanoparticles, Pharm. Res. 21 (2004) 1818–1825.

[10] N.A. Belsey, N.L. Garrett, L.R. Contreras-Rojas, A.J. Pickup-Gerlaugh, G.J. Price, J. Moger, R.H. Guy, Evaluation of drug delivery to intact and porated skin by coherent Raman scattering and fluorescence microscopies, J. Control. Release 174 (2014) 37–42.

[11] W.S. Chiu, N.A. Belsey, N.L. Garrett, J. Moger, M.B. Delgado-Charro, R.H. Guy, Molecular diffusion in the human nail measured by stimulated Raman scattering microscopy, Proc. Natl. Acad. Sci. U. S. A. 112 (2015) 7725–7730.

[12] M. Vettor, S. Bourgeois, H. Fessi, J. Pelletier, P. Perugini, F. Pavanetto, M.A. Bolzinger, Skin absorption studies of octyl-methoxycinnamate loaded poly(D,L-lactide) nanoparticles: estimation of the UV filter distribution and release behaviour in skin layers, J. Microencapsul. 27 (2010) 253–262.

[13] K. Hashimoto, Ultrastructure of the human toenail. Cell migration, keratinization and formation of the intercellular cement, Arch. Dermatol. Forsch. 240 (1970) 1–22.

[14] H. Germann, W. Barran, G. Plewig, Morphology of corneocytes from human nail plates, J. Investig. Dermatol. 74 (1980) 115–118.

[15] K.A. Walters, G.L. Flynn, Permeability characteristics of the human nail plate, Int. J. Cosmet. Sci. 5 (1983) 231–246.

[16] D. Mertin, B.C. Lippold, In-vitro permeability of the human nail and of a keratin membrane from bovine hooves: influence of the partition coefficient octanol/water and the water solubility of drugs on their permeability and maximum flux, J. Pharm. Pharmacol. 49 (1997) 30–34.

[17] Y. Kobayashi, T. Komatsu, M. Sumi, S. Numajiri, M. Miyamoto, D. Kobayashi, K. Sugibayashi, Y. Morimoto, In vitro permeation of several drugs through the human nail plate: relationship between physicochemical properties and nail permeability of drugs, Eur. J. Pharm. Sci. 21 (2004) 471–477.

[18] J.C. Garson, F. Baltenneck, F. Leroy, C. Riekel, M. Muller, Histological structure of human nail as studied by synchrotron X-ray microdiffraction, Cell. Mol. Biol. 46 (2000) 1025–1034.

[19] K. Hashimoto, Cementsome, a new interpretation of the membrane-coating granule, Arch. Dermatol. Forsch. 240 (1971) 349–364.

[20] J. Dutet, M.B. Delgado-Charro, Assessment of iontophoretic and passive ungual penetration by laser scanning confocal microscopy, Pharm. Res. 29 (2012) 3464–3474.

[21] B.L. Lewis, H. Montgomery, The senile nail, J. Investig. Dermatol. 24 (1955) 11–18.

[22] X. Wu, G.J. Price, R.H. Guy, Disposition of nanoparticles and an associated lipophilic permeant following topical application to the skin, Mol. Pharm. 6 (2009) 1441–1448.

[23] B.I. Olvera-Martinez, J. Cazares-Delgadillo, S.B. Calderilla-Fajardo, R. Villalobos-Garcia, A. Ganem-Quintanar, D. Quintanar-Guerrero, Preparation of polymeric nanocapsules containing octyl methoxycinnamate by the emulsification–diffusion technique: penetration across the stratum corneum, J. Pharm. Sci. 94 (2005) 1552–1559.

[24] R. Alvarez-Roman, G. Barre, R.H. Guy, H. Fessi, Biodegradable polymer nanocapsules containing a sunscreen agent: preparation and photoprotection, Eur. J. Pharm. Biopharm. 52 (2001) 191–195.

[25] J.C. Mansfield, G.R. Littlejohn, M.P. Seymour, R.J. Lind, S. Perfect, J. Moger, Label-free chemically specific imaging in planta with stimulated Raman scattering microscopy, Anal. Chem. 85 (2013) 5055–5063.